Fabrication of a translational photoacoustic needle sensing probe for interstitial photoacoustic spectral analysis

Wei-Kuan Lin [a], Linyu Ni [b], Xueding Wang [b,c], Jay L. Guo [a], Guan Xu [b,d,*]

[a] Department of Electrical Engineering and Computer Sciences, University of Michigan, 1301 Beal Avenue, Ann Arbor, MI, USA
[b] Department of Biomedical Engineering, University of Michigan, 2200 Bonisteel Blvd, Ann Arbor, MI, USA
[c] Department of Radiology, University of Michigan, 1301 Catherine St, Ann Arbor, MI, USA
[d] Department of Ophthalmology and Visual Sciences, University of Michigan, 1000 Wall St, Ann Arbor, MI, USA

ARTICLE INFO

ABSTRACT

In our previous study, we demonstrated the feasibility of using an all-optical interstitial photoacoustic (PA) needle sensing probe for quantitative study of tissue architectures with PA spectral analysis (PASA). In this work, we integrated the optical components into an 18 G steel needle sheath for clinical translation. The dimensions of the needle probe are identical to those of a core biopsy probe and are fully compatible with standard procedures such as prostate biopsy. To our knowledge, this is the first interstitial PA probe that can acquire signals with sufficient temporal length for statistics-based PASA. We treated the inner surface of the steel needle sheath and successfully suppressed the vibrational PA signals generated at the surface. Purposed at boosting the measurement sensitivity and extending sensing volume, we upgraded the Fabry-Pérot hydrophone with a plano-concave structure. The performance of the translational needle PA sensing probe was examined with phantoms containing microspheres. The trend of the linear spectral slopes shows negatively correlated to the microsphere dimensions while the midband-fits are positively correlated to microsphere diameters and concentrations. The PASA quantifications show the ability to differentiate microspheres with varied dimensions.

1. Introduction

Microscopic tissue architecture is a critical component in the pathological diagnosis of diseases [1]. The standard procedure for accessing tissue microarchitecture is core biopsy followed by histopathology [2, 3]. However, biopsy is invasive and is frequently accompanied with complications, and the histopathology of the extracted tissue samples is time and effort demanding [4]. Photoacoustic (PA) imaging, taking advantage of the unique optical absorption spectra of individual tissue components, and the ultrasonics resolution and penetration, has demonstrated the capability in resolving tissue architectures formed by tissue components such as hemoglobin, lipid, and collagen [5–9].

PA spectral analysis (PASA), recently investigated by a few research groups including us, has achieved quantification of tissue microarchitectures without tissue extraction [10–19]. During PASA, the power spectrum of PA signals is calculated and fitted to a linear function. The slope of the linear function represents the relative magnitude of the high frequency signal components compared with that of the low frequency ones, which is correlated with the dimensions of the tissue

architectures generating the PA signals. And the overall magnitude of the linear-fit represents the concentration of the targeted tissue component within the assessed volume. PASA has successfully quantified tissue architectures formed by nucleic acid, hemoglobin, lipid and collagen, taking advantage of their unique optical absorption at the optical wavelengths of 266 nm, 800 nm, 1220 nm and 1370 nm, respectively.

PASA requires extensive signal length in time domain and spectral bandwidth in frequency domain for reliable statistical analysis. Purposed at avoiding attenuation to the PA signals along the propagation path, we developed an interstitial measurement approach [12,19]. Instead of acquiring 2-D or 3-D images using an ultrasound transducer array positioned far from the region of interest (ROI), a needle probe was inserted into the ROI. The needle probe consists of a fiber-optic diffuser for illuminating a large tissue volume and a needle hydrophone for capturing the broadband PA signals. We iterated through a few prototypes of the needle probe, from a large-diameter design combining manually polished optical fiber and piezo-electric needle hydrophones, to a slim all-optical design integrating fiber-optic diffuser with

---

controlled etching and microfabricated Fabry-P é rot fiber-optic hydrophone. The performance of the needle was examined with rodent prostates in vivo [11] and canine and human prostates *ex vivo* [11,14]. The results of these studies show promise of the technology in quantifying the architectural changes during the progression of the prostate cancer [12,14,19]. Currently a large majority of biopsy cores from the prostates are normal tissue. However, clinicians only need to sample the most aggressive location to make a clinical decision. The ultimate application of this proposed needle probe in prostate cancer diagnosis is to 1) locate the aggressive cancer location without tissue extraction; and 2) guide biopsy extraction only in the aggressive region for confirmed pathology. The needle will be used in a multiple insertion approach. Although the optical and acoustic attenuations from the sensing volume are intertwined in a 1-D measurement, the insertions close or within the tumor region will produce quantitative measurements with strongest indication of cancer [20]. With such a localization approach, biopsy core extractions only need to be performed at limited locations.

Purposed at translating the technology to clinics, the miniaturization and integration of PA measurement components into a standard clinical needle is necessary. As mentioned above, the prototype needle PA probes were mostly validated in detecting prostate cancer [12,14,19]. This study focuses on integrating the PA measurement components into a needle sheath that is compatible with prostate biopsy procedure. Several requirements and limitations need to be considered. 1) The acoustic detector needs to fit into a needle with dimensions of a standard 18 G biopsy needle, which we have achieved by using a fiber-optic hydrophone in a previous study [19]. 2) The hydrophone should have high sensitivity despite the small sensing element. 3) Broad frequency

bandwidth (~20 MHz) is necessary for resolving fine microscopic architectures in tissue. 4) The delivery of PA illumination needs to be maximized to enhance signal intensity. 5) PA signals generated by the needle sheath should be minimized to ensure sufficient signal-to-noise ratio (SNR). 6) A large effective measurement volume is desired, which is determined by the illumination and signal detection sensitivity in combination. To address the issues, we upgraded the commercial planar fiber-optic hydrophone to a plano-concave design. The microfabrication process was fully in-house following the procedures established in a pioneering study [21]. With a geometry that provides better quality factor and wider receiving angle, the plano-concave fiber-optic hydrophone substantially increases the sensing volume of the needle PA probe. In addition, we treated the inner surface of needle sheath with polymer and gold coating to minimize PA signal generation at the surface and maximize the illumination delivery efficiency.

The translational needle PA probes were examined with phantoms including microspheres with controlled concentrations and dimensions. The PASA quantifications of the acquired signals show the ability to differentiate microspheres with varied dimensions. The trend of the linear spectral slopes and midband-fits of different microsphere diameters and concentrations quantified from the measurements by the translational needle PA probe matched with our previous results [15].

2. Materials and methods

2.1. Overview of needle PA sensing probe

Fig. 1(a) depicts the overview of the translational PA system
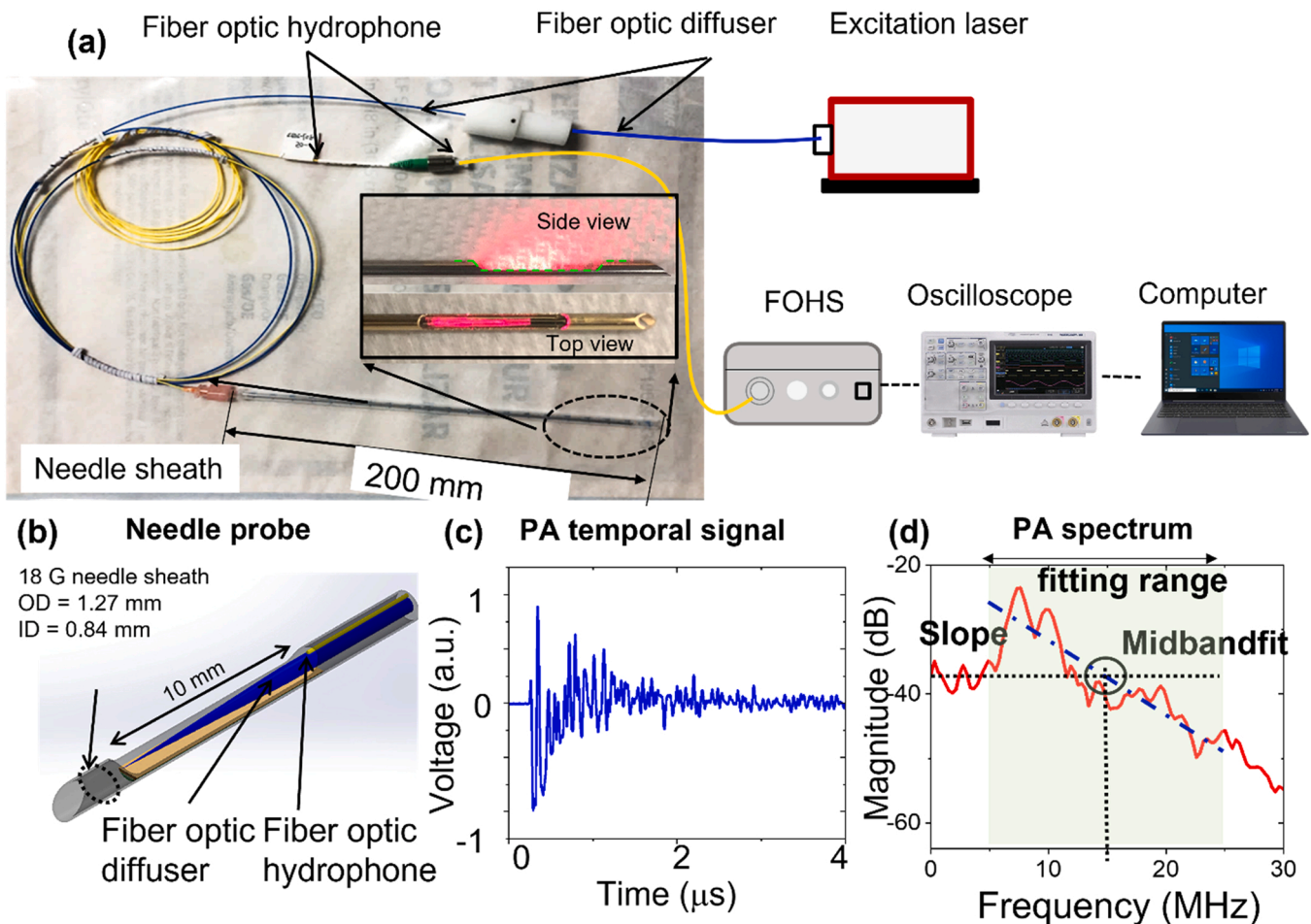

Fig. 1. Overview of the needle PA probe system. (a) The experimental setup of the PASA needle probe system. (b) The sketch of the needle probe. (c) The PA signal in time domain. (d) The PA spectrum and the quantitative PASA quantifications.

including the needle probe, composed of a fiber-optic hydrophone, a fiber-optic diffuser and the needle sheath, the excitation laser, the fiber-optic hydrophone data acquisition system, the oscilloscope and a computer. The detailed sketch of the needle probe is shown in Fig. 1(b). A fiber-optic hydrophone and a fiber-optic diffuser were integrated into a 200-mm long, 18-gauge needle sheath with an outer diameter of 1.27 mm and an inner diameter of 0.84 mm, and a cutout of 12 mm × 1 mm for exposing the optical components.

The photoacoustic illumination was achieved by the excitation laser and the fiber-optic diffuser. The output of a pulsed Nd:YAG laser (532 nm, 5–7 ns pulse width, 10 Hz repetition rate, Q-smart, Quantel, France) was coupled into the fiber-optic diffuser. 532 nm laser has stable output, which helps reducing uncertainties during this study on the performance of our new device. The fiber-optic diffuser was fabricated by dipping the emission end of an optical fiber into Hydrofluoric acid ≤48 % (HF, Sigma-Aldrich, Cleveland, OH) at a rate of approximately 0.55 μm per second [22]. At the end of the fabrication procedure, the emission end of the optical fiber is etched into a conical shape with a length of 6 mm and only emits illumination in the azimuthal dimension of the fiber. The optical density at the emission surface is controlled below 2 mJ to ensure the output from the cutout window is under 20 mJ/cm^2 to meet the safety limit established by American National Standard Institute (ANSI).

The PA signal detection was achieved by a fiber-optic hydrophone and a data acquisition system (PrecisionAcoustics, UK). For the fiber-optic hydrophone, a Fabry-Pérot (F-P) structure was fabricated on the tip of a 125 μm optical fiber, where two mirrors sandwiched a flexible polymer layer. The fabrication of the fiber-optic hydrophone is described in detail in the next section. The other end of the optical fiber was coupled to the data acquisition system, where a tunable interrogation laser operated near 1550 nm. Due to the resonant feature of F-P structure, reflectivity can rapidly change as the thickness of the polymer varies with the acoustic vibration at the resonant optical wavelength. The reflected laser power acquired by the fiber-optic hydrophone was digitized by an oscilloscope (MDO3000, Tektronix, TX) as a measurement of PA signals, as shown in Fig. 1(c). The signals were then sent into a computer for PASA. Fig. 1(d) illustrates the PASA method. During PASA the signal power spectra within a frequency-range-of-interest is fit to a linear model, which captures the descending trend of the spectral magnitude as the frequency increases. Midband-fit is quantified as the magnitude of the linear fit at the middle of the fitting range. Therefore, midband-fit is a representation of the overall volume or concentration in unit volume of optical absorbing materials. In contrast, slope represents the relative magnitude of the high frequency signals components to the low ones. Slopes are mostly related to the dimensions of the optical absorbers instead of the total volume.

2.2. Fiber-optic hydrophone

2.2.1. Fabrication of the fiber-optic hydrophone

In our previous studies, we investigated an all-optical design for the needle PA sensing probe using commercially available fiber-optic hydrophones with planar F-P structures (Precision Acoustics, UK) [23,24]. In this study, we improved the performance of the all-optical needle PA probe using a fiber-optic hydrophone with a plano-concave F-P structure. We developed protocols for fabricating both the planar and plano-concave hydrophones in-house following the procedures described in [21,25]. Fig. 2(a) shows the structures of the two hydrophones. As illustrated in Fig. 2(a), compared to the planar design, the concave reflection surface in the plano-concave structure avoids optical
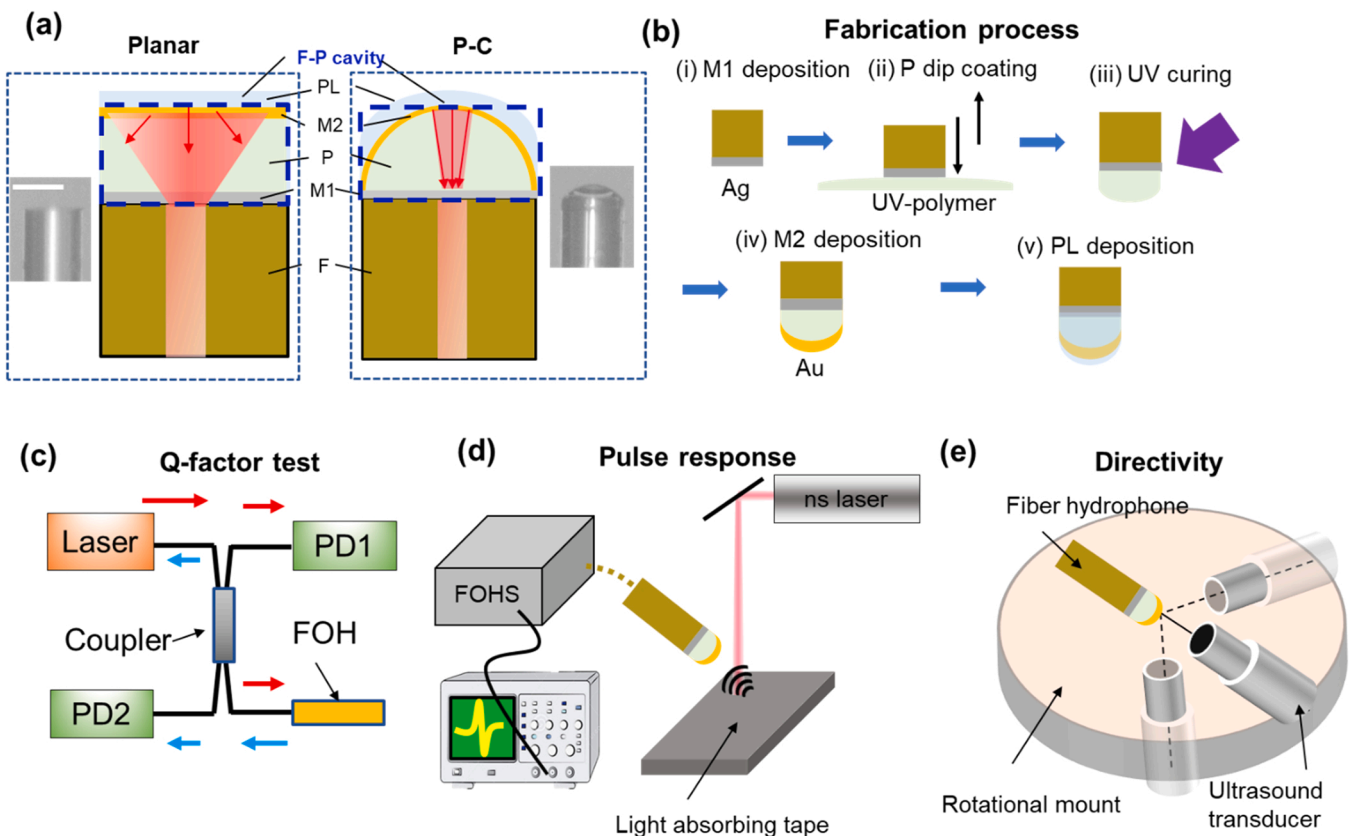

Fig. 2. Fabrication and characterization of the fiber-optic hydrophones. (a) The structures of planar and plano-concave fiber hydrophones. (b) Fabrication process of the fiber-optic hydrophone. (i) M1 deposition with Ag; (ii) Polymer layer by dip coating with U-V polymer; (iii) UV curing; (iv) M2 deposition with Au; (v) Protection layer coating. (c) Setup for quality (Q) factor measurement. (d) Setup of pulse response test of the fiber-optic hydrophone. (e) Setup of sensing directivity test of the fiber hydrophones. P-C: plano-concave, M: mirror, P: polymer, PL: protection layer, F-P: Fabry-Pérot, PD: photodetector, FOH: fiber-optic hydrophone.

loss due to beam walk-off issue, and thus enhances sensitivity and lowers the noise-equivalent-pressure (NEP). The concave surface also allows for a wider reception angle, which will be shown in the results section.

Planar F-P structure has two flat mirrors and a spacer between them. The first mirror is a 20-nm Ag film deposited on the tip of a 125-μm single mode fiber (P3-SMF28Y-FC-5, Thorlabs, NJ) using evaporation process (EvoVac, Angstrom Engineering, USA). The spacer is a 10-μm parylene layer deposited through physical vapor deposition (PDS 2035CR, Specialty Coating Systems, USA). The second mirror is a 100 nm Au film also deposited using evaporation process.

For the plano-concave structure, the fabrication procedure is based on the procedures described [21]. We developed our own fabrication protocol, as depicted in Fig. 2(b). A layer of 20-mm Ag was deposited on the cleaved fiber tip as first mirror (M1) (i). Then, the optical fiber was dipped into UV-polymer liquid (NOA61, Norland Optical Adhesive) and pulled out, forming a dome shaped polymer layer (ii). After curing by UV light (iii), another layer of 100-nm gold layer was deposited on top of the domed spacer surface, forming the second concave mirror (M2) (iv). Both the planar and the plano-concave F-P structures were packaged by depositing 5 μm parylene as a protection layer (PL) (v).

2.2.2. Characterization of the fiber-optic hydrophone

The fabricated hydrophones were first tested for their quality (Q) factor with the setup shown in Fig. 2(c). A tunable laser (Velocity TLB6728, Newfocus, USA) was directed into a 2×2 50:50 fiber coupler (TN1550R5A2, Thorlabs). The laser energy coupled into the fiber hydrophone was monitored by a photodetector (PD1). The light reflected from the fiber hydrophone was recorded by another photodetector (PD2). The reflectivity spectrum was then obtained by dividing the readings from PD2 with the readings from PD1 and normalized by the maximum reflectivity. With the reflectivity spectrum, the Q factor was quantified as the ratio of central wavelength and the full-width at half maximum of the reflectivity dip. Larger Q factor indicates lower NEP and better sensitivity.

Next, the impulse response of the fiber hydrophone was tested and the setup is illustrated in Fig. 2(d). The fiber-optic hydrophone was positioned 1 mm away from and perpendicular to the surface of a piece of black tape. Both tape and the hydrophone were submerged into water. PA signals were generated by the previously mentioned 532 nm laser. Considering the high optical absorption of the black tape, optical energy can barely penetrate into the tape. Therefore, PA signal is only generated at the surface and can be considered as a narrow impulse to the fiber-optic hydrophone with a broad frequency bandwidth. The impulse responses of both planar and plano-concave hydrophones were acquired at a sampling rate of 250 MHz. The noise-equivalent pressure of the plano-concave fiber-optic hydrophone is also quantified by applying ~ 50 kPa pressure at 10 MHz with US transducer (A312S-SU, Olympus) pre-calibrated by a hydrophone (HNC-1500, ONDA).

Finally, the directivity of fiber hydrophone was quantified. As shown in Fig. 2(e), a 10 MHz ultrasound transducer (V317, Olympus, Center Valley, PA) is fixed in a water tank. The fiber hydrophone was mounted on a rotational stage, facing toward the transducer. The fiber hydrophone swept from -90 degree to $+90$ degree relative to the transducer and the maximum signal magnitudes were plot as a function of the receiving angles.

2.3. Needle sheath design and optimization

Fig. 3(a) shows the sketch of the needle sheath with (i) cross-section and (ii) side views. As discussed in Section 2.1, the needle sheath has a cutout for exposing the optical components of the needle PA probe (10 mm $\times$ 1 mm). Purposed at minimizing the PA signals generated at the inner surface of the needle sheath, a reflection surface was fabricated. The inner wall of the needle at the cutout was dispensed with 0.5 μL of 90 °C polymer layer (NOA61, Norland Optical Adhesive, USA). Due to low surface tension at high temperature, the UV polymer will form a ~100 μm thick polymer layer that produces a smooth surface. The polymer was then cured under UV light for 15 min and a 100-nm gold film was deposited on the polymer surface, forming a mirror with 96 % reflectivity. Because of gravity, the polymer layer and the gold coating are flat, as illustrated in Fig. 3(a). Such design minimizes the PA signals generated at the inner wall of the needle and maximizes the optical energy delivered into the assessed volume [26]. The relative positions of the fiber-optic diffuser, the fiber-optic hydrophone and the cutout on the needle are fixed using medical grade silicone glue (MasterSil 151Med, Masterbond, Hackensack, NJ). The thin layer of silicone glue avoids the contact between the microfabricated components and the human tissue.

2.4. Fiber needle system characterization

Firstly, we tested the effects of the needle sheath treatment on the measurement noise. The total noise level (n_t) of the measurement can be expressed as $n_t = \sqrt{n_v^2 + n_s^2}$ [27], where n_v is vibrational noise, i.e. the PA signals generated at the needle sheath inner surface by the diffusive illumination, and n_s is the system noise caused by laser fluctuation and electronic noises, etc. It is worth noting that n_v is from the vibration of the needle sheath and cannot be eliminated by purely optimizing the hydrophone design. To characterize n_v, needle PA probes with three configurations were tested, including 1) untreated needle sheath inner surface; 2) polished needle sheath inner surface with gold coating; and 3) needle sheath inner surface with gold coating on top of a smoothened polymer layer.

The output of the above-mentioned 532 nm laser was collimated and delivered to the coupling end of the illumination fiber. The output optical density from the needle PA system was 3 mJ/cm^2. The probes were immersed in water. Measurements were acquired with sampling rate of 250 MHz with no average and the first 20 μs of the signal was recorded. Since no optical absorbing object was placed in the detection regime, the recorded data were purely noise. By taking the root mean square of the
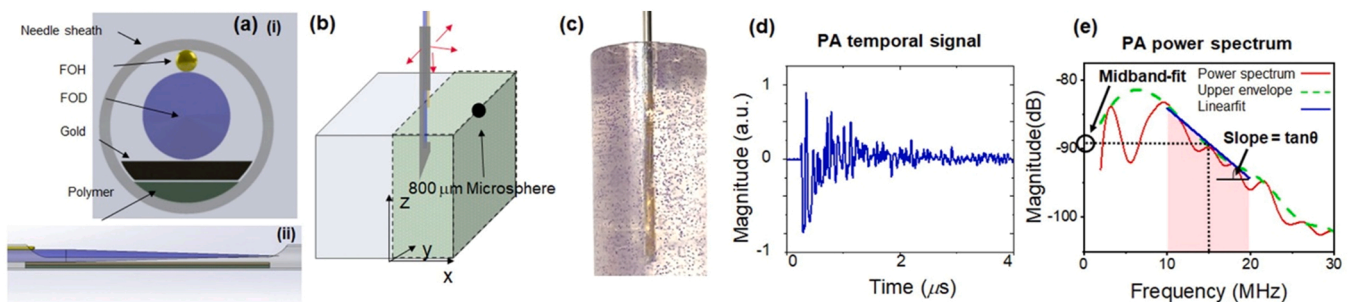

Fig. 3. Design of the needle probe and setups for performance characterization. (a) sketch of the PASA probe with (i) cross-section and (ii) side view. (b) Setup for characterizing the sensing volume of the PASA needle probe. (c) A picture of a microsphere phantom for testing the needle probe. FOH: fiber-optic hydrophone, FOD: fiber-optic diffuser. (d) Representative PA signals. (e) PA power spectrum and illustration of PASA.

data, n_t can be obtained. Because of the relative positions of the needle sheath and the sensing fiber, n_v only appeared in the first 8 μs (i.e. the length of the cutout window, 10 mm) and n_s was the only noise source from 8 μs to 20 μs. Therefore, n_s can be obtained by taking n_t from 8 to 20 μs and n_v can be acquired by taking $\sqrt{n_t^2 - n_s^2}$ from 0 to 8 μs.

Next, we tested the sensing volume of the needle PA probe. In this experiment, both planar hydrophone and plano-concave fiber hydrophone were examined for comparison. The setup is illustrated in Fig. 3 (b). An 800-μm microsphere (UVPMS-BV, Fisher scientific LLC., Santa Barbara, California) was fixed at the tip of a positioning fiber. The PA needle probe was mounted on a 3D stage. Both the needle probe and the microsphere were submerged in water. The same optical energy and data acquisition settings were used except that each measurement was averaged 64 times. The probe was moved at step size 0.5 mm and PA signals were obtained at every scanning step. SNR were quantified as the ratio of the peak-to-peak value of the PA signal from the microsphere over that of the background noise. The collected data were then presented in a 3D SNR map. The detection volume of the needle probe was defined as the spatial range where SNR is larger than 1.

2.5. PASA study of microsphere phantom

The needle probe was then tested in generating reliable measurements for PASA. As shown in Fig. 3(c), cylindrical phantoms were fabricated with polyethylene microspheres (UVPMS-BV, Fisher scientific LLC., Santa Barbara, California) uniformly and randomly distributed in 10 % porcine gel (G2500, Sigma-Aldrich Co. LLC., Burlington, MA). Illumination at 532 nm is well absorbed by the purple microspheres. We fabricated 12 phantoms, including 100, 200 and 400 μm-diameter microspheres at concentrations of 1, 2, 4, and 8 microspheres per mm³.) For each phantom, 20 measurements were taken at separated locations

in the phantom, resulting in a total of 240 independent measurements.

Fig. 3(d) shows a typical signal in time domain. Purposed at excluding the signals generated at the inner needle surface, only the signals in the range of 1 μs to 5 μs was used. The frequency domain power spectrum of the signals was calculated using MATLAB built-in function, pwelch, as shown in Fig. 3(e). The power spectrum was compensated using the frequency response of the hydrophone shown later in Fig. 4(b,ii). However, the effects of the stop bands of the frequency response of the hydrophone cannot be completely removed, leading to the fluctuations in the power spectrum. To generate a smooth spectral profile for quantification, the upper envelope of the signal power spectra was calculated, as shown in Fig. 3(e). Then, the envelope within a selected range (10–20 MHz unless specified) was fitted to a linear model. The spectral slopes and midband-fits, as illustrated in Fig. 3(e), were compared with the dimensions and concentrations of the microspheres in the phantoms. Correlation coefficients (r) between linear slopes/midband-fits and particle sizes/concentrations were calculated. T-tests with the null hypothesis that the microspheres cannot be differentiated by PASA parameters were performed. We also tested the influence of the linear fitting range on the PASA results. The midband-fits and slopes derived from the frequency ranges of 10–15 MHz, 10–20 MHz, 10–25 MHz, and 10–30 MHz were compared.

3. Results

3.1. Fiber hydrophone characterization

Fig. 4(a) shows the reflectivity spectrum. The planar fiber hydrophone shows a 7-nm FWHM of the reflectivity dip, corresponding to a Q factor of approximately 221. In contrast, the FWHM demonstrated by the plano-concave design is 0.6 nm with a Q factor of approximately
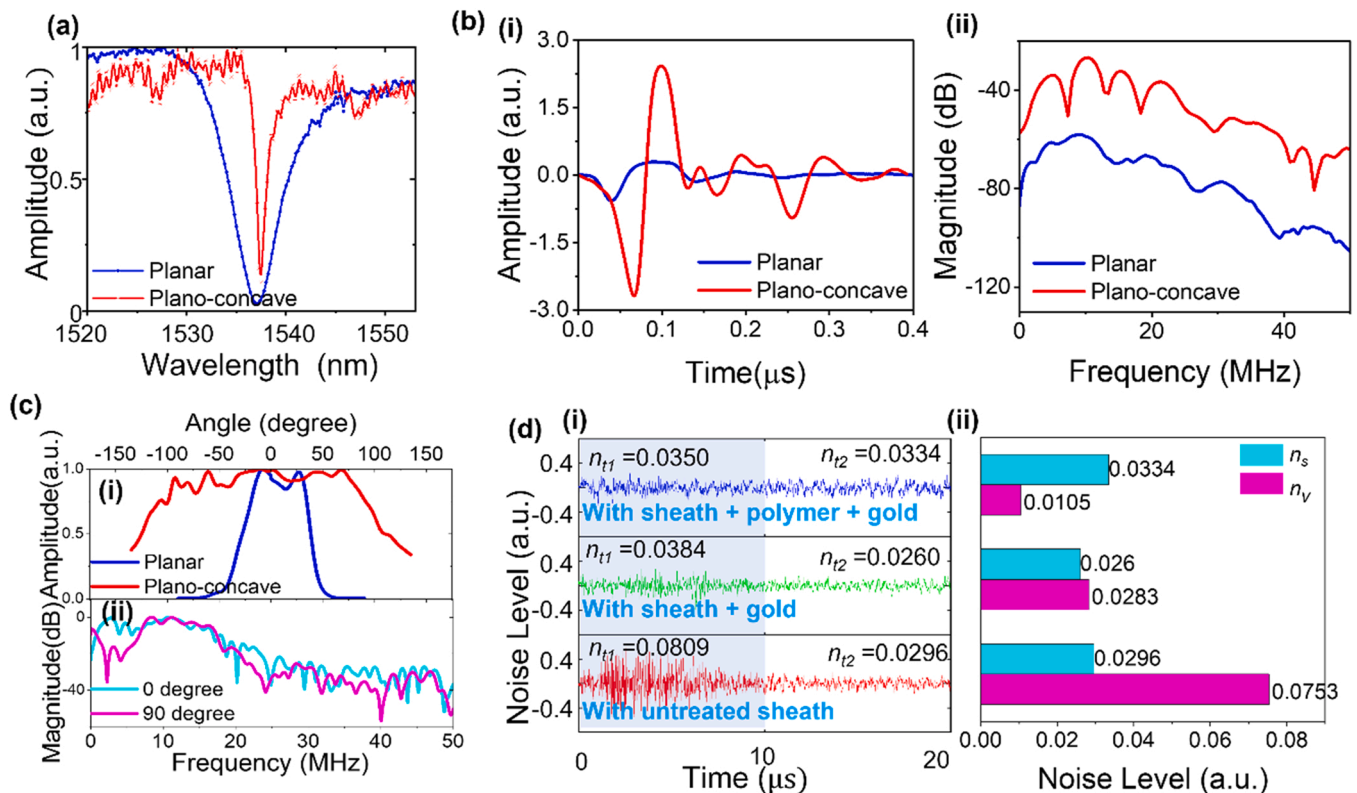

Fig. 4. Performance of the fiber hydrophone and the needle PA probe. (a) Reflectivity spectra of F-P structures at the tip of the fiber-optic hydrophones. (b,i) The impulse responses of the fiber-optic hydrophones in time domain. (b, ii) The impulse responses in frequency domain. (c) The directivity functions of the planar and plano-concave fiber hydrophones. (d, i) The time domain signals acquired by needle PA probe with varied treatment to the needle sheath inner surface. (d, ii) The n_v and n_s of the needle sheath configurations in (d, i).

2583. The Q factor improvement for more than 11 times can result in approximate 11-time signal strength.

The impulse response of the needle hydrophones is shown in Fig. 4 (b). Fig. 4(b, i) demonstrates the vibrational signal detected in time domain. Here, with the same excitation pulse energy, the plano-concave hydrophone shows peak amplitude with 2.42 V and the planar one with only 0.42 V. The measured NEP of the hydrophones are ~0.2 kPa and ~ 1.6 kPa for plano-concave and planar hydrophones, respectively. There numbers are comparable to the results shown in ref. [30,31]. By taking the Fourier transform, we can obtain the corresponding frequency domain power spectrum as shown in Fig. 4(b, ii). Both hydrophones show relatively flat spectrum within 5 – 20 MHz, which is sufficiently wide for PASA analysis.

Fig. 4(c) compares the angular sensitivity of planar and plano-concave fiber hydrophones. The plano-concave fiber hydrophone demonstrates almost the same sensitivity across the range between −100 and 100 degrees. In contrast, the planar one shows highest sensitivity at the forward direction while sensitivity drops below 0.5 when the detection angle is larger than 30 degrees. Fig. 4(c, ii) shows the frequency responses at the 0 degree and 90 degree respectively. Both have relatively flat spectrum within 10–30 MHz, indicating the spectrum is not a strong function with respect to the receiving angle.

3.2. Performance of the needle sheath coating

The noise test result is shown in Fig. 4(d). The measured total noise from 0 to 8 μs and 12–20 μs is denoted as n_{t1} and n_{t2} respectively. In the case of untreated needle sheath (red), the measured n_{t1} and n_{t2} are 0.0809 V and 0.0296 V. The surface polishing and gold film deposited on the needle sheath (green) reduce n_{t1} and n_{t2} to 0.0384 V and 0.0260 V, respectively. For the case of needle sheath with smooth polymer layer and gold film (blue), n_{t1} further reduces to 0.0350 V, and n_{t2} is at approximately the same level as the other two cases. With n_{t1} and n_{t2}, we obtained the vibrational noise (n_v), i.e. PA signal intensity generated at the needle sheath inner surface, and system noise (n_s), as shown in Fig. 4(d, ii). n_s is relatively stable at ~ 0.3 V level. However, it can be clearly seen that the n_v reduced from 0.0753 V in the case without treatment to 0.0105 V after treatment with polymer and gold coating, demonstrating more than 7 times noise reduction. After treatment n_v is 3 times lower than n_s, indicating the total noise is mainly from the system noise.

3.3. Sampling volume of the needle PA probes

Fig. 5(a) and (b) show the 3D SNR maps of the PA needle probes with the planar and plano-concave fiber hydrophones, respectively. For the probe with planar hydrophone, the highest SNR is 11 dB, when the sphere was right next to the sensor. In contrast, the plano-concave hydrophone shows a highest SNR of 30 dB, meaning that the SNR is ~ 10 times higher than the planar one. We approximated the detection volumes (defined above as locations where SNR is larger than 1) of both hydrophones with a quarter ellipsoid. As illustrated in Fig. 5(a) and (b), the detection volumes are determined as $(\frac{4}{3}\pi \times 1.5 \times 1.5 \times 4 \times \frac{1}{4}) = 9.4\text{mm}^3$ and $(\frac{4}{3}\pi \times 3 \times 4 \times 6 \times \frac{1}{4}) = 75.4\text{ mm}^3$ for the planar and plano-concave fiber hydrophones, respectively. With the improved sensitivity, the sensing volume of the needle PA probe with the plano-concave fiber
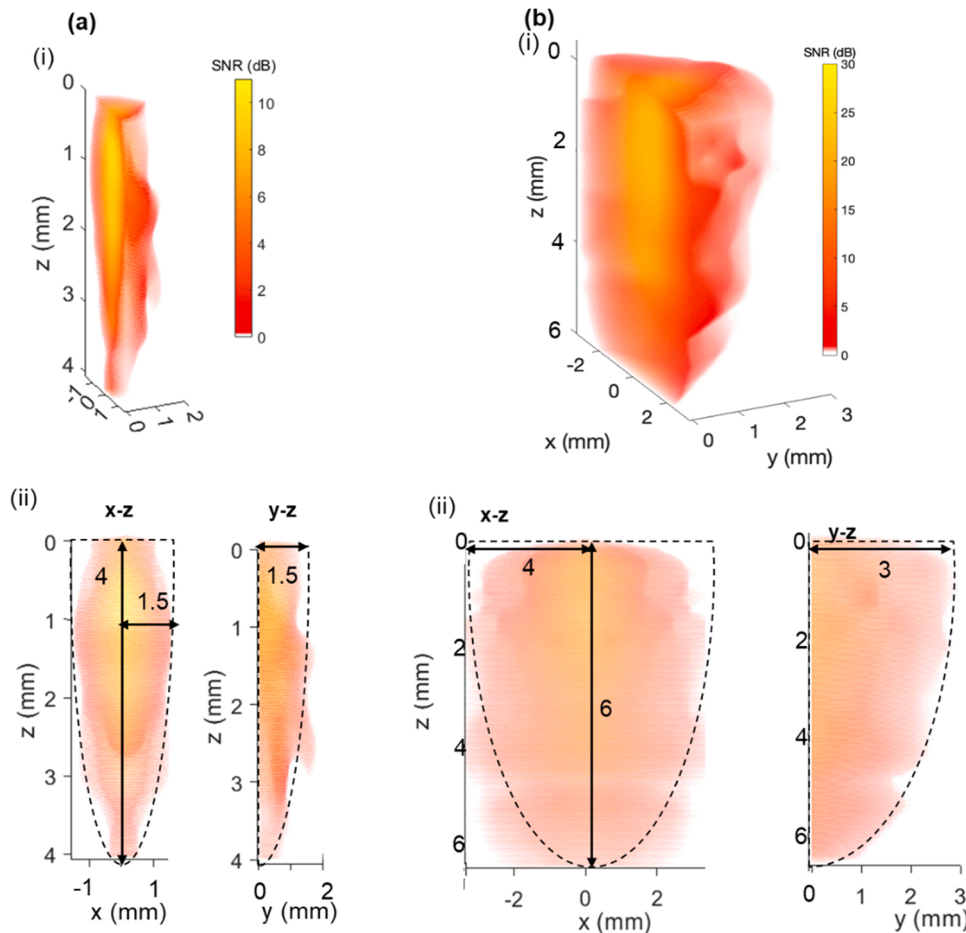

Fig. 5. SNR maps of the PASA needle probes. (a) Needle probe with planar hydrophone and (b) with plano-concave hydrophone of (i) 3D map and (ii) 2D x-z and y-z maps. Dotted lines indicate the approximated contour of SNR = 1.

hydrophone is 8 times larger than that with the planar one.

3.4. PASA results in phantom study

Fig. 6(a) and (b) are the representative time domain PA signals and the corresponding power spectra, respectively. The shaded area in the Fig. 6(a) indicates the windowed time sequence that is used for spectral study. Fig. 6(b) shows strong correlations ($r^2 > 0.9$) between the upper envelopes of the signal power spectra and the fitted linear functions.

Fig. 6(c) and (d) show the statistical results of the spectral slopes and the spectral midband-fits derived from phantoms containing microspheres with 3 different diameters and 4 different concentrations. The linear spectral slopes in Fig. 6(c) show strong and negative correlations with the dimensions of the microspheres (n = 20, p << 0.05 for all concentrations), while not correlate to particle concentration. Fig. 6(d) shows that midband-fits are positively correlated to particle concentration (n = 20, p << 0.05 for all sizes) and particle sizes. These findings agree with our theoretical analysis [29] mentioned in the introduction section.

Fig. 6(e) and (f) show the influences of the window selection on the slopes and midband-fits. Fig. 6(e) shows that the negative correlation relation between slopes and particle diameters can be always obtained in the fitting ranges, although the absolute value of slopes might be different. Fig. 6(f) shows that the positive correlation relation between midband-fits and particle concentration are also maintained in different window selection. The results indicate the robustness of the spectral analysis method.

Table 1 shows that PASA slopes can be used to differentiate between the dimensions of the microspheres with significance in most cases. Table 2 shows that PASA midband-fits can be used to differentiate between the concentrations of the microspheres with significance, although with less reliability. These results agree with our previous findings in [28,29].

Table 1
Differentiating microsphere dimensions by PASA slopes.

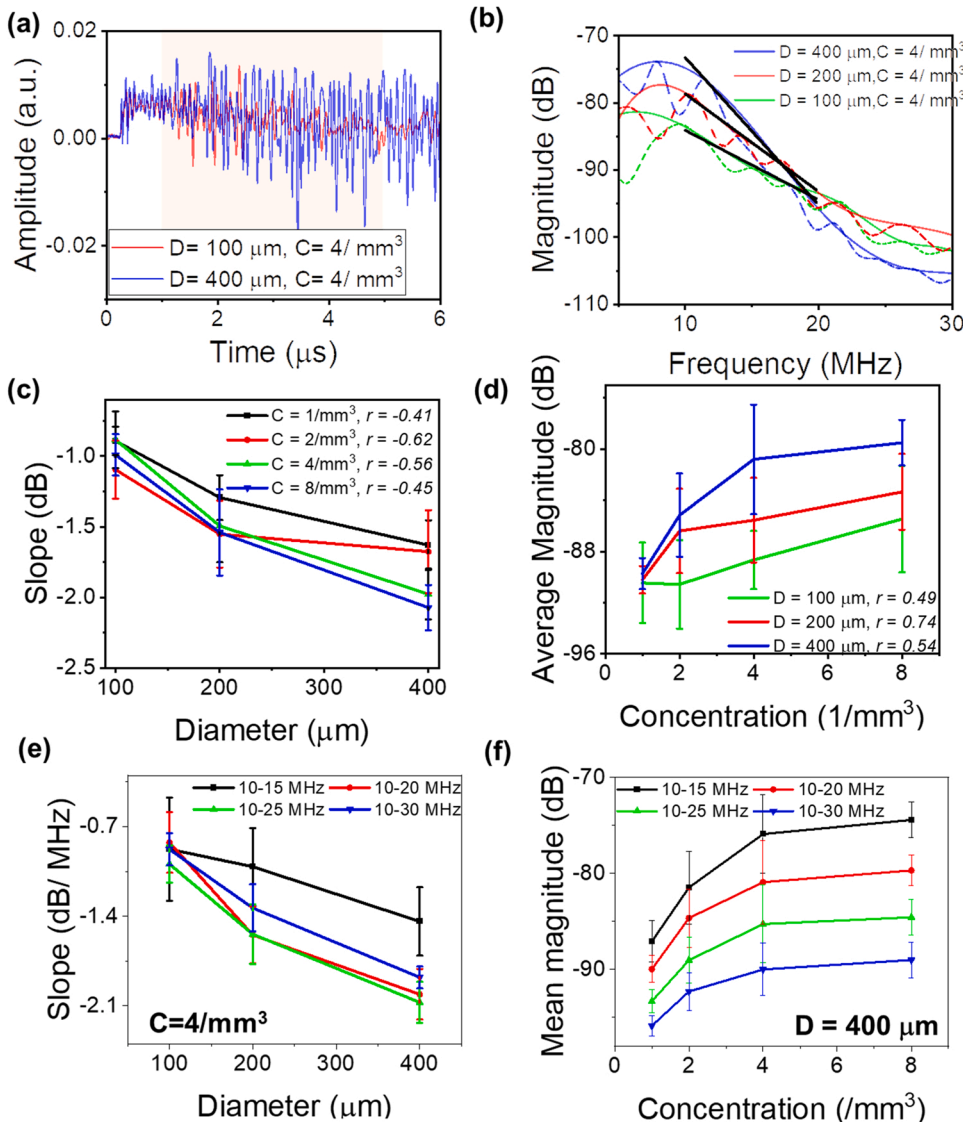| Concentrations (number of microspheres per mm³)	100 vs 200 (μm)	200 vs 400 (μm)	100 vs 400 (μm)
1	<0.01	<0.01	<0.01
2	<0.01	0.3572	<0.01
4	<0.01	0.01	0.095
8	<0.01	<0.01	<0.01

Fig. 6. Results of phantom study. (a) Representative time-domain PA signals from the phantoms. (d) Representative power spectra of signals acquired from the phantoms. (c)-(d): Statistics of (c) linear spectra slopes and (d) midband-fits of microsphere phantoms with different diameters and concentrations. (e)-(f): Statistics of (e) linear spectra slopes with different diameters and fitting range at 4/mm³ concentration and (f) midband-fits of 400 μm diameter microsphere phantoms with different concentrations and fitting ranges at samples.

Table 2

Differentiating microsphere concentrations by PASA midband-fits (groups without p-value >0.05 in any combination, i.e., are not shown).

Diameters (μm)	1 vs 2 per mm^3	2 vs 4 per mm^3	2 vs 8 per mm^3
100	0.5	0.05	0.02
200	<0.01	0.20	0.05
400	<0.01	<0.01	<,0.01

4. Discussion

As illustrated in Fig. 4(a), the design with concave surface significantly improved the Q factor of F-P resonator, resulting in a huge improvement of NEP compared to the planar surface design. On the acoustic signal detection side, the concave surface allows for wide angle signal reception. The sensitivity of the fiber hydrophone can be further enhanced by increasing the sensor Q factor, such as replacing the lossy metal mirrors with the low loss dielectric based distributed Bragg reflectors [21,30] or using other sensing method such as whispering gallery mode [32–34]. As shown in Fig. 4(c), the fiber hydrophone has a wide receiving angle (-90 to 90 degree), while the needle window is only open on one side. Therefore, part of the hydrophone receiving angle is blocked by the needle sheath and the fiber-optic hydrophone collects vibrational noise generated at the inner surface of the needle sheath. In this case, side sensing elements, such as angled fiber F-P sensors and whispering gallery modes [35,36] as mentioned above, will be considered in future studies.

The gold coating on top of a smooth polymer layer, by suppressing the PA signal generated at the inner surface of the needle sheath, effectively improved the SNR of the system. In addition, the highly reflective coating at the inner surface assists more efficient illumination delivery through the needle probe and, therefore, better penetration of the measurements. Coupled with the plano-concave fiber-optic hydrophone, the needle PA probe demonstrates a larger sampling volume compared to the prototype version [14].

The current single element sensor can only provide averaged measurements within the whole assessed volume. Measurements at multiple locations with the needle PA probe may provide a spatial distribution of the microarchitectures. One potential way to improve the spatial resolution of the interstitial measurement is to incorporate multiple sensors into the system, such as using a bundle of fiber hydrophones or an array of micro-fabricated pressure sensors [37–39], which will be investigated in our future works.

Although calibrated by the frequency response of the Fabry-P é rot sensor, the signal power spectra in this study show low magnitudes at characteristic frequencies, leading to fluctuating spectra. An envelope detection method is implemented before the linear fitting process in the PASA. This approach showed excellent robustness in producing consistent results in multiple frequency ranges. In addition, the Fabry-P é rot sensor in this study cannot fully capture the low frequency signal components. The midband-fits, i.e. the magnitudes of the linear-fit to the signal spectra in the middle of the fitting range, may not precisely represent the total volume of the light absorption material. Therefore, midband-fits show moderate correlations with the concentrations and limited reliability in differentiating the microsphere concentrations.

Since the phantoms contain multiple microspheres in a large volume, attenuation compensation is difficult. In the experiment setup, we ensure that the phantom volumes are sufficiently large, so that the full measurement range of the needle probe contains microspheres with uniform randomness. Such design ensured the consistent attenuation factor and the comparability in all measurements. Time-gating was also performed to limit the PASA within a spatial range, which reduced the dependence on the attenuation to signals generated far from the sensor.

The aggregation and exceedingly high concentration of the microspheres may increase the low frequency components in the PA signals. Theoretically, the spatial resolution of a transducer is determined as

speed of sound divided by its acoustic bandwidth. In this study, the highest frequency we can reach is 30 MHz. Therefore, the system cannot resolve two microspheres if the separation is 50 μm. This corresponds to the concentration of 512, 64 and 8 per cm^3 for microspheres with diameters of 100 μm, 200 μm and 400 μm, respectively. The concentrations used in this study is far lower than these values.

5. Conclusion

In conclusion, we have developed a translational needle PA sensing probe with identical dimensions of a clinical biopsy needle. Compared to the previous versions, this needle probe possesses upgraded components including a needle sheath with a highly reflective inner surface that protects the optical components and greatly reduces PA signals generated by the needle sheath. A plano-concave F-P fiber-optic hydrophone is also introduced for improved signal reception. The needle PA probe was tested in phantom studies and the results indicate that the probe can statistically distinguish different concentration and sizes of microsphere samples. To our understanding, this is the first interstitial PA probe that can acquire signals with sufficient temporal length for statistics-based PASA. This work paves the way for examining the technology inhuman subjects.

Declaration of Competing Interest

The authors have no conflict of interest to disclose.

Data Availability

Data will be made available on request.

Acknowledgements

References

[1] V. Kumar, Abul K. Abbas, Jon C. Aster, Jerrold R. Turner, Pathologic Basis of disease tenth edition (2015) 1328.

[2] D. Joy, V.R. Thava, B.B. Scott, Diagnosis of fatty liver disease, Eur. J. Gastroenterol. Hepatol. 15 (2003) 539–543, https://doi.org/10.1097/01.meg.0000059112.41030.2e.

[3] L. Gortzak-Uzan, W. Jimenez, S. Nofech-Mozes, N. Ismiil, M.A. Khalifa, V. Dubé, B. Rosen, J. Murphy, S. Laframboise, A. Covens, Sentinel lymph node biopsy vs. pelvic lymphadenectomy in early stage cervical cancer: Is it time to change the gold standard? Gynecol. Oncol. 116 (2010) 28–32, https://doi.org/10.1016/J.YGYNO.2009.10.049.

[4] S. Loeb, S. van den Heuvel, X. Zhu, C.H. Bangma, F.H. Schröder, M.J. Roobol, Infectious complications and hospital admissions after prostate biopsy in a european randomized trial, Eur. Urol. 61 (2012) 1110–1114, https://doi.org/10.1016/J.EURURO.2011.12.058.

[5] P. Beard, Biomedical photoacoustic imaging, Interface Focus 1 (2011) 602–631, https://doi.org/10.1098/RSFS.2011.0028.

[6] E. Hysi, R.K. Saha, M.C. Kolios, Photoacoustic ultrasound spectroscopy for assessing red blood cell aggregation and oxygenation, J. Biomed. Opt. 17 (2012), 125006, https://doi.org/10.1117/1.JBO.17.12.125006.

[7] Y. Pu, W. Wang, G. Tang, R.R. Alfano, Changes of collagen and nicotinamide adenine dinucleotide in human cancerous and normal prostate tissues studied using native fluorescence spectroscopy with selective excitation wavelength, J. Biomed. Opt. 15 (2010), 047008, https://doi.org/10.1117/1.3463479.

[8] L. v Wang, S. Hu, Photoacoustic tomography: in vivo imaging from organelles to organs, Science 335 (2012) (1979) 1458–1462, https://doi.org/10.1126/SCIENCE.1216210/ASSET/1B81424F-201D-408E-B8A1-252E1B67268E/ASSETS/GRAPHIC/335_1458_F3.JPEG.

[9] L. v Wang, Multiscale photoacoustic microscopy and computed tomography, Nat. Publ. Group 3 (2009), https://doi.org/10.1038/nphoton.2009.157.

[10] G. Xu, M.C. Davis, J. Siddiqui, S.A. Tomlins, S. Huang, L.P. Kunju, J.T. Wei, X. Wang, Quantifying Gleason scores with photoacoustic spectral analysis: feasibility study with human tissues, Biomed. Opt. Express 6 (2015) 4781, https://doi.org/10.1364/BOE.6.004781.

[11] J. Jo, J. Siddiqui, Y. Zhu, L. Ni, S.-R. Kothapalli, S.A. Tomlins, J.T. Wei, E.T. Keller, A.M. Udager, X. Wang, G. Xu, Photoacoustic spectral analysis at ultraviolet wavelengths for characterizing the Gleason grades of prostate cancer, Opt. Lett. 45 (2020) 6042, https://doi.org/10.1364/OL.409249.

[12] H. Zhang, W. Chao, Q. Cheng, S. Huang, X. Wang, D. Wu, G. Xu, Interstitial photoacoustic spectral analysis: instrumentation and validation, Biomed. Opt. Express 8 (2017) 1689, https://doi.org/10.1364/boe.8.001689.

[13] E. Amidi, A. Mostafa, S. Nandy, G. Yang, W. Middleton, C. Siegel, Q. Zhu, Classification of human ovarian cancer using functional, spectral, and imaging features obtained from in vivo photoacoustic imaging, Biomed. Opt. Express 10 (2019) 2303, https://doi.org/10.1364/BOE.10.002303.

[14] L. Ni, J. Siddiqui, A.M. Udager, J. Jo, J.T. Wei, M.S. Davenport, P.L. Carson, J. B. Fowlkes, X. Wang, X. Wang, X. Wang, G. Xu, G. Xu, G. Xu, Characterizing the aggressiveness of prostate cancer using an all-optical needle photoacoustic sensing probe: feasibility study, Opt. Soc. Am. (2021), https://doi.org/10.1364/BOE.430085.

[15] G. Xu, J.B. Fowlkes, C. Tao, X. Liu, X. Wang, Photoacoustic spectrum analysis for microstructure characterization in biological tissue: Analytical model, Ultrasound Med Biol. 41 (2015) 1473–1480, https://doi.org/10.1016/J.ULTRASMEDBIO.2015.01.010.

[16] G. Xu, I.A. Dar, C. Tao, X. Liu, C.X. Deng, X. Wang, Photoacoustic spectrum analysis for microstructure characterization in biological tissue: A feasibility study, Appl. Phys. Lett. 101 (2012), https://doi.org/10.1063/1.4768703.

[17] T. Feng, Q. Li, C. Zhang, G. Xu, L.J. Guo, J. Yuan, X. Wang, Characterizing cellular morphology by photoacoustic spectrum analysis with an ultra-broadband optical ultrasonic detector, Opt. Express 24 (2016) 19853, https://doi.org/10.1364/OE.24.019853.

[18] G. Xu, Z.X. Meng, J.D. Lin, J. Yuan, P.L. Carson, B. Joshi, X. Wang, The functional pitch of an organ: Quantification of tissue texture with photoacoustic spectrum analysis, Radiology 271 (2014) 248–254, https://doi.org/10.1148/radiol.13130777.

[19] S. Huang, Y. Qin, Y. Chen, J. Pan, C. Xu, D. Wu, W.Y. Chao, J.T. Wei, S.A. Tomlins, X. Wang, J.B. Fowlkes, P.L. Carson, Q. Cheng, G. Xu, Interstitial assessment of aggressive prostate cancer by physio-chemical photoacoustics: An ex vivo study with intact human prostates, Med. Phys. 45 (2018) 4125–4132, https://doi.org/10.1002/mp.13061.

[20] L. Ni, W. kuan Lin, A. Kasputis, D. Postiff, J. Siddiqui, M.J. Allaway, M. S. Davenport, J.T. Wei, J.L. Guo, T.M. Morgan, A.M. Udager, X. Wang, G. Xu, Assessment of prostate cancer progression using a translational needle photoacoustic sensing probe: Preliminary study with intact human prostates ex-vivo, Photoacoustics 28 (2022), https://doi.org/10.1016/J.PACS.2022.100418.

[21] J.A. Guggenheim, J. Li, T.J. Allen, R.J. Colchester, S. Noimark, O. Ogunlade, I. P. Parkin, I. Papakonstantinou, A.E. Desjardins, E.Z. Zhang, P.C. Beard, Ultrasensitive plano-concave optical microresonators for ultrasound sensing, Nat. Photonics 11 (2017) 714–719, https://doi.org/10.1038/s41566-017-0027-x.

[22] W.-H. Choi, I. Papautsky, Fabrication of a needle-type pH sensor by selective electrodeposition, Https://Doi.Org/10.1117/1.3580751. 10 (2011) 020501. https://doi.org/10.1117/1.3580751.

[23] E.Z. Zhang, P.C. Beard, A miniature all-optical photoacoustic imaging probe, Photons Plus Ultrasound.: Imaging Sens. 2011 7899 (2011) 78991F, https://doi.org/10.1117/12.874883.

[24] P. Morris, A. Hurrell, A. Shaw, E. Zhang, P. Beard, A Fabry–Pérot fiber-optic ultrasonic hydrophone for the simultaneous measurement of temperature and acoustic pressure, J. Acoust. Soc. Am. 125 (2009) 3611–3622, https://doi.org/10.1121/1.3117437.

[25] E.Z. Zhang, P.C. Beard, Characteristics of optimized fibre-optic ultrasound receivers for minimally invasive photoacoustic detection, Photons Plus Ultrasound.: Imaging Sens. 2015 9323 (2015), 932311, https://doi.org/10.1117/12.2081904.

[26] D. Bergström, J. Powell, A.F.H. Kaplan, The absorption of light by rough metal surfaces—a three-dimensional ray-tracing analysis, J. Appl. Phys. 103 (2008), 103515, https://doi.org/10.1063/1.2930808.

[27] D. Fitzpatrick, Noise Analysis, Analog Design and Simulation Using OrCAD Capture and PSpice. (2018) 197–208. https://doi.org/10.1016/B978-0-08-102505-5.00014–8.

[28] G. Xu, J.B. Fowlkes, C. Tao, X. Liu, X. Wang, Photoacoustic spectrum analysis for microstructure characterization in biological tissue: Analytical model, Ultrasound Med. Biol. 41 (2015) 1473–1480, https://doi.org/10.1016/J.ULTRASMEDBIO.2015.01.010.

[29] G. Xu, I.A. Dar, C. Tao, X. Liu, C.X. Deng, X. Wang, Photoacoustic spectrum analysis for microstructure characterization in biological tissue: a feasibility study, Appl. Phys. Lett. 101 (2012), 221102, https://doi.org/10.1063/1.4768703.

[30] B. Chen, Y. Chen, C. Ma, Photothermally tunable Fabry-Pérot fiber interferometer for photoacoustic mesoscopy, Biomed. Opt. Express 11 (2020) 2607, https://doi.org/10.1364/boe.391980.

[31] G. Li, Z. Guo, S.-L. Chen, Miniature all-optical probe for large synthetic aperture photoacoustic-ultrasound imaging, Opt. Express 25 (2017) 25023, https://doi.org/10.1364/oe.25.025023.

[32] B. Fu, Y. Cheng, C. Shang, J. Li, G. Wang, C. Zhang, J. Sun, J. Ma, X. Ji, B. He, Optical ultrasound sensors for photoacoustic imaging: a narrative review, Quant. Imaging Med. Surg. 12 (2022) 1608–1631, https://doi.org/10.21037/qims-21-605.

[33] C. Zhang, T. Ling, S.L. Chen, L.J. Guo, Ultrabroad bandwidth and highly sensitive optical ultrasonic detector for photoacoustic imaging, ACS Photonics 1 (2014) 1093–1098, https://doi.org/10.1021/ph500159g.

[34] X. Jiang, A.J. Qavi, S.H. Huang, L. Yang, Whispering-gallery sensors, Matter 3 (2020) 371–392, https://doi.org/10.1016/J.MATT.2020.07.008.

[35] H. Bae, H. Liu, M. Yu, X.M. Zhang, Miniature surface-mountable Fabry–Perot pressure sensor constructed with a 45 degree angled fiber, Opt. Lett. 35 (10) (2010) 1701–1703, https://doi.org/10.1364/OL.35.001701.

[36] B. Luo, L. Yan, L. Li, Q. Wu, W. Pan, X. Zou, X. Zhang, Angled fiber-based Fabry–Perot interferometer, Opt. Lett. 45 (2) (2020) 292–295, https://doi.org/10.1364/OL.45.000292.

[37] R. Ansari, E.Z. Zhang, A.E. Desjardins, P.C. Beard, All-optical forward-viewing photoacoustic probe for high-resolution 3D endoscopy, Light Sci. Appl. 7 (2018) 1–9, https://doi.org/10.1038/s41377-018-0070-5.

[38] R. Ansari, E.Z. Zhang, A.E. Desjardins, P.C. Beard, Miniature all-optical flexible forward-viewing photoacoustic endoscopy probe for surgical guidance, Opt. Lett. 45 (2020) 6238, https://doi.org/10.1364/ol.400295.

[39] W.J. Westerveld, M. Mahmud-Ul-Hasan, R. Shnaiderman, V. Ntziachristos, X. Rottenberg, S. Severi, V. Rochus, Sensitive, small, broadband and scalable optomechanical ultrasound sensor in silicon photonics, Nat. Photonics 15 (2021) 341–345, https://doi.org/10.1038/s41566-021-00776-0.

Wei-Kuan Lin received the Bachelor's and Master's degree in physics from National Taiwan University, Taiwan. He is currently working toward the Ph.D. degree in Electrical and Computer Engineering in the University of Michigan. His research interests include photoacoustic imaging, optical sensors design and fabrication, and fiber optics and photonics.

Linyu Ni she received her Ph.D. student in Biomedical Engineering at the University of Michigan, Ann Arbor. Her primary research interests are photoacoustic microscopy and clinical applications of photoacoustic imaging.

Xueding Wang is Professor at the Department of Biomedical Engineering, University of Michigan, holding an adjunct Professor position at the Department of Radiology. Before working as an independent principal investigator, Dr. Wang received his Ph.D. from the DDwight Look College of Engineering at Texas A \&M University, and then finished postdoctoral training at the University of Michigan School of Medicine. Dr. Wang has extensive experience in imaging system development and adaptation of novel diagnostic technology to laboratory research and clinical managements, especially those involving light and ultrasound. Sponsored by NIH, NSF, DoD and other funding agencies, his research has led to over 120 + peer-reviewed publications. At the University of Michigan Medical School, a major part of his research is focused on clinical applications of photoacoustic imaging, including those involving arthritis, prostate cancer, liver conditions, breast cancer, Crohn's disease, and eye diseases. Dr. Wang is the recipient of the Sontag Foundation Fellow of the Arthritis National Research Foundation in 2005, and the Distinguished Investigator Award of the Academy of Radiology Research in 2013. He is also sitting on the editorial boards of scientific journals including Photoacoustics, Journal of Biomedical Optics, Medical Physics, and Ultrasonic Imaging, and being the steering committee member of the Journal of Lightwave Technology.
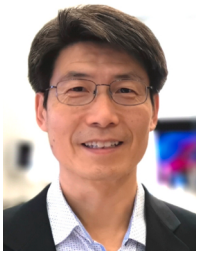
Jay Guo started his academic career at the University of Michigan in 1999 and is currently a professor of Electrical Engineering and Computer Science, with joint appointment in Applied Physics, Mechanical Engineering, Macomolecular Science and Engineering. He has 190 refereed journal publications with over 13,500 citations. Many published works from his lab have been reported by numerous media. His group's research includes polymer-based photonic devices and sensor applications, laser generated ultrasound, organic and hybrid photovoltaics, plasmonic nanophotonics, and roll to roll nanomanufacturing technologies.
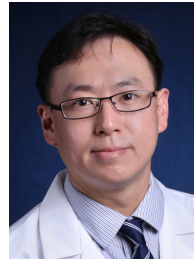
Guan Xu received his PhD and postdoctoral training in optical and ultrasound imaging in biomedicine. He received a pre-doctoral award from Congressionally Directed Medical Research Programs, a postdoctoral fellowship from American Heart Association, a Career Development Award from American Gastroenterology Association, a Senior Research Award from Crohn's and Colitis Foundation and an R37 MERIT award from National Cancer Institute.